

Polycyclic Aromatic Hydrocarbons (PAHs) in the High-redshift Universe: Prospect of the PRIMA FIRESS low-resolution spectroscopy

Ilsang Yoon^{1,2,*}, Brandon Hensley³, Thomas S. -Y. Lai⁴, Irene Shivaiei⁵, Ismael García-Bernete⁶, Grant P. Donnelly⁷, Alexandra Pope⁸, J. D. T. Smith⁷, Paul Torrey²

¹National Radio Astronomy Observatory, 520 Edgemont Road, Charlottesville, VA 22903, USA

²Department of Astronomy, University of Virginia, P.O. Box 3818, Charlottesville, VA 22903, USA

³Jet Propulsion Laboratory, California Institute of Technology, 4800 Oak Grove Drive, Pasadena, CA 91109, USA

⁴IPAC, California Institute of Technology, 1200 E. California Blvd., Pasadena, CA 91125

⁵Centro de Astrobiología (CAB), CSIC-INTA, Carretera de Ajalvir km 4, Torrejón de Ardoz, 28850, Madrid, Spain

⁶Centro de Astrobiología (CAB), CSIC-INTA, Camino Bajo del Castillo s/n, E-28692 Villanueva de la Cañada, Madrid, Spain

⁷Ritter Astrophysical Research Center, University of Toledo, Toledo, OH 43606, USA

⁸Department of Astronomy, University of Massachusetts, Amherst, MA 01003, USA

Abstract. The integrated luminosity from the features of the polycyclic aromatic hydrocarbons (PAHs) exceeds the luminosity from atomic and molecular emission lines in the star-forming regions in galaxies and is a potential tracer of galaxy-scale star formation and molecular gas content of the high-redshift universe. We simulate the observable PAH spectra using the PROBE far-Infrared Mission for Astrophysics far-infrared enhanced survey spectrometer (FIRESS) and investigate the capability of the FIRESS low-resolution spectroscopy for observing PAH emission spectrum from high-redshift galaxies. Our investigation suggests that (1) PRIMA observations of PAH emission are $\gtrsim 10$ times more efficient at detecting galaxies than the VLA observations of CO(1-0) for galaxies with the same infrared luminosity, (2) PRIMA/FIRESS can detect the PAH emission from galaxies with $L_{\text{IR}} \sim 10^{12} L_{\odot}$ up to the end of reionization (and possibly beyond, if $L_{\text{IR}} \sim 10^{13} L_{\odot}$), (3) the PAH band ratios measured from a full spectral fitting and from a simple flux “clipping” method are different and vary depending on the interstellar radiation field strength, and (4) PRIMA/FIRESS can also be used as the PAH mapping instrument to measure star formation and redshift of the galaxies in high-redshift protoclusters.

Keywords: spectrometer, far-infrared, high-redshift galaxies, dust, PAH.

*Ilsang Yoon, iyoon@nrao.edu

1 Introduction

One of the key quests in studying galaxy formation and evolution is tracing cosmic star formation and the molecular gas content (i.e., fuel for star formation) as a function of redshift from the present to the epoch of the first galaxy formation. Different parts of the electromagnetic spectrum (emission lines and continuum) trace different ‘faces’ of star formation (SF): the ultraviolet (UV) and optical spectrum trace the young stellar populations and surrounding ionized medium, while the radio and far-infrared (FIR) spectrum trace the dust, atoms, and molecules mainly heated by nearby SF (see Madau & Dickinson 2014¹ for review of the cosmic star formation history).

Traditionally, carbon monoxide (CO) has been used as a tracer of molecular gas content because the CO molecule—the second most abundant (after H_2) molecule in a galaxy’s interstellar medium (ISM)—is excited by collision with H_2 molecules (i.e., star-forming material) in star-forming molecular clouds. The Kennicutt-Schmidt (KS) relation² captures the connection between molecular gas and SF. As a result, the CO emission is known to be well correlated with the distribution of molecular gas and the IR luminosity (a tracer of SF) for galaxies in the nearby^{3–5} and

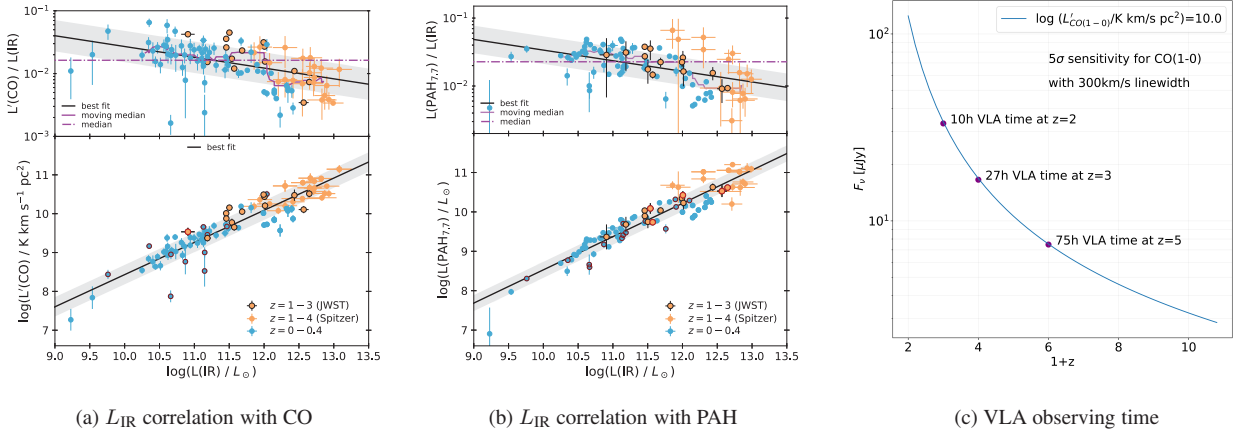


Fig 1 Panel (a) and (b): Correlation of L_{IR} with CO(1-0) and with PAH_{7.7} luminosity for nearby and distant galaxies (up to $z = 4$). Figures are created using the data from Shivaie & Boogaard 2024.²³ Panel (c): VLA 5σ sensitivity with 300 km s⁻¹ bandwidth for a galaxy with $L'_{\text{CO}(1-0)} = 10^{10} \text{ K km s}^{-1} \text{ pc}^2$ to be detected in CO(1-0) as a function of redshift. The VLA observing time (including overhead) estimates are shown at $z=2, 3$, and 5.

distant⁶⁻¹¹ Universe. Although, under the assumption of thermal equilibrium in the star-forming molecular gas, the increasing brightness of CO with higher J rotational transitions is an advantage for observing high-redshift galaxies as demonstrated by the use of radio-millimeter-FIR observing facilities (e.g., VLA, ALMA, NOEMA), the lowest transition line, CO(1-0) with the X_{CO} factor¹²(i.e., a conversion factor between CO line brightness and H₂ column density), is the best tracer of the total molecular gas mass.

Another useful tracer of SF is the mid-IR (MIR) emission from Polycyclic Aromatic Hydrocarbon (PAH) molecules^{13,14} which absorb UV and optical photons from star-forming regions and supply the bulk of the photoelectrons responsible for heating interstellar gas.¹⁵ Although the AGN feedback in AGN-host galaxy also affects the PAH emission from a central ≈ 100 pc region,¹⁶⁻²⁰ the integrated PAH emission from 1 – 10 kpc² scale in strongly star-forming galaxies can be as large as up to 20% of the galaxy's total infrared luminosity,²¹ which makes it a potentially efficient way of detecting galaxies in high-redshift as already suggested by the previous observations of the Spitzer space telescope.²²

From the KS relation, one can expect a correlation between PAHs, CO molecules, and star formation rate (SFR). As shown in the previous literature, CO(1-0) luminosity obtained either from direct measurement or conversion from higher- J rotational transitions, is correlated with the total IR luminosity (for example, Fig. 1(a)) that traces SFR. However, PAH emission is also well correlated with the total IR luminosity^{24,25} as shown in Fig. 1(b) as an example. The PAH emission correlates strongly with CO emission at sub-kiloparsec scales over diverse environments of local star-forming and active galactic nucleus (AGN) host galaxies,²⁶⁻²⁸ with an indication of stronger correlation than that of CO-SFR or PAH-SFR.²⁹ The PAH-CO connection is also seen beyond the local Universe.^{23,30,31} Based on the compilations of large samples of galaxies with both mid-infrared spectroscopy and CO observations,^{21,30,32} a universal PAH-CO correlation is found from $z \sim 0$ to $z \sim 4$ on galaxy integrated scales.³¹

However, observing CO(1-0) becomes difficult with increasing redshift. To illustrate this dif-

difficulty, we estimate the VLA 5σ sensitivity for CO(1-0) observation from a galaxy with $L'_{\text{CO(1-0)}} = 10^{10} \text{ K km s}^{-1} \text{ pc}^{-2}$ (and the corresponding IR luminosity $L_{\text{IR}} = 10^{12} L_{\odot}$) by assuming a linewidth for sensitivity estimate to be 300 km s^{-1} .⁶ Fig. 1(c) shows the 5σ RMS sensitivity for CO(1-0) as a function of the galaxy redshift. We also present the total VLA observing time (including calibration) for the corresponding sensitivity at $z = 2, 3, 5$. It is clear that even at $z = 3$, the observing time (≈ 30 hours) is already significantly large and the CO(1-0) observation is not practically feasible if galaxies are at $z > 4$. Furthermore, at high redshift, the CMB temperature ($T(z) = 2.73 \times (1 + z)$) is comparable to or can be even higher than the typical CO excitation temperature ($T_{\text{CO(1-0)}} \sim 10 - 20 \text{ K}$ ³³). Thus, the contrast between the observed CO brightness and the CMB background decreases with redshift,³⁴ making the observing situation worse. Given the challenges in observing CO from high-redshift galaxies, one may consider the PAH emission as an alternative to CO to trace the star-forming galaxies across cosmic time: from cosmic noon ($z = 2-4$) to cosmic dawn ($z \sim 10$).

In the post-Spitzer era, JWST/MIRI Medium Resolution Spectroscopy (MRS) is the only instrument capable of observing PAH emission spectrum from high-redshift galaxies. It already has a showcase: $3.3\mu\text{m}$ PAH emission spectrum from a lensed star-forming galaxy at $z = 4.22$,³⁵ and the ongoing JWST/MIRI MRS programs will observe PAH emission spectra from star-forming galaxies (e.g., GO-5279, PI: Shivaei) and AGNs (e.g., GO-3158, PI: Mainieri) at cosmic noon. However, the dramatically decreasing sensitivity of JWST/MIRI in the long wavelength channels (channel 4 in MIRI/MRS) and the degraded performance of the MRS long wavelength channels due to a time-dependent evolution in the effective count rateⁱ, do not allow for probing PAH emission from galaxies at $z > 4$.

The next generation far-infrared space telescope, PRobe far-Infrared Mission for Astrophysicsⁱⁱ (PRIMA) is a 1.8 meter diameter, cryogenically-cooled to 4.5K, far-infrared observatory concept for the community in the 2030 decade, and includes both a sensitive wideband spectrometer, Far-InfraRed Enhanced Survey Spectrometer (FIRESS) and a multi-band spectrophotometric imager/polarimeter, PRIMA imager (PRIMAger). The PRIMA/FIRESS is an ideal instrument to observe PAH emission spectrum from galaxies up to the end of reionization and possibly beyond, as proposed in, for example, chapters 18, 21, and 22 in the PRIMA GO science book.³⁶ Moreover, the wavelength range and the sensitivity of PRIMA/FIRESS complement the JWST/MIRI MRS, enabling characterization of the spectrum with the full set of PAH bands for galaxies in the nearby and distant Universe. In this paper, we simulate an ensemble of the noise-added PAH spectra for PRIMA/FIRESS to observe galaxies in a wide range of redshift and different PAH properties, investigate the redshift limit for detection, and compare the PAH luminosity measurement from the full spectrum using all four bands and a segment of the spectrum from a single band.

2 Simulating Observable PAH Spectrum

We create a suite of simulated spectra of the PAH and dust grains heated by an interstellar radiation field and compare the observed flux density to the sensitivity of the PRIMA/FIRESS with low-resolution mode. In this section, we describe the methods and assumptions in our simulation.

ⁱ <https://www.stsci.edu/contents/news/jwst/2023/temporal-behavior-of-the-miri-reduced-count-rate>

ⁱⁱ <https://prima.ipac.caltech.edu/>

Table 1 FIRESS Base Grating Module Instrument Parameters³⁷

Parameter	Band 1	Band 2	Band 3	Band 4
Spectral Range (μm)	24 – 43	42 – 76	74 – 134	130 – 235
Spectral Sampling (μm)	0.23	0.41	0.73	1.29
Resolving Power	90 – 150	85 – 120	90 – 125	95 – 130
Pixel Size on Sky (arcsec)	7.6	7.6	12.7	22.9
Line Sensitivity [†] (W/m^{-2})	1.9×10^{-19}	1.9×10^{-19}	1.9×10^{-19}	1.9×10^{-19}
Continuum Sensitivity [‡] (μJy)	64	125	196	193

[†] 5σ point source sensitivity in 1-hour integration for an unresolved line

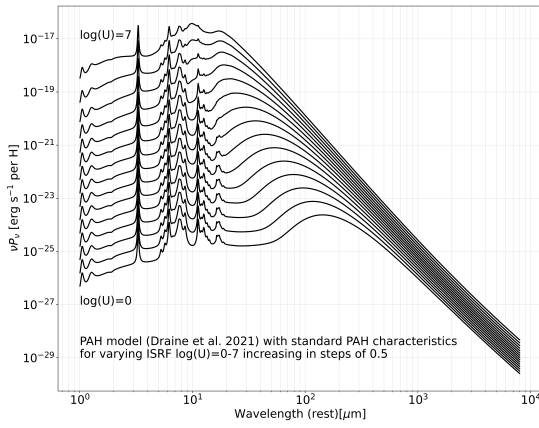
[‡] 5σ point source sensitivity in 1-hour integration for $R = 10$ binning, estimated by PRIMA ETC

2.1 Model PAH emissivity

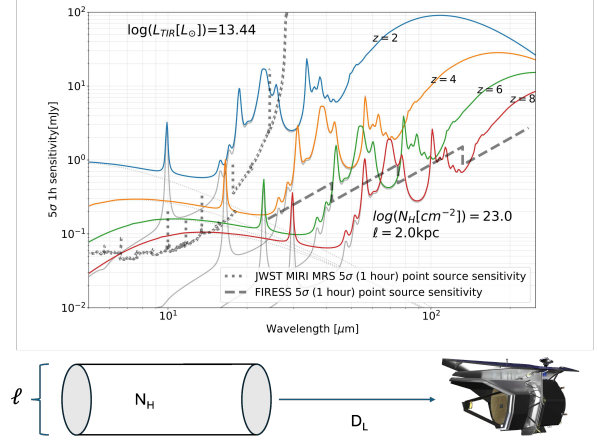
A recent study by Draine et al., 2021³⁸ calculates the dust emission including PAHs for a range of the physical parameters of ISM and dust grains to provide the models for interpreting PAH spectra measured by ISO, Spitzer, AKARI, and JWST. We find that this library of PAH model spectra is also useful for simulating PAH spectra observed by PRIMA FIRESS. The spectrum of model PAH emissivity, νP_ν (erg s⁻¹ per H atom) is computed for a given set of parameters: spectral type of interstellar radiation field (ISRF), grain size distribution, PAH mass fraction (q_{PAH}), PAH ionization fraction, scale parameter of ISRF strength (U) relative to the one in the solar neighborhood.³⁸ The total IR emissivity (L_{IR}) for dust and PAHs is also computed based on the choice of ISRF. For more detailed information, see Draine et al., 2021.³⁸

Fig. 2(a) presents the emissivity spectra of PAH and dust grains,³⁸ νP_ν for a range of ISRF strength U ($1 < U < 10^7$) for the ISRF spectrum in the solar neighborhood (mMMP³⁹), ‘standard’ⁱⁱⁱ grain size distribution, PAH mass fraction ($q_{\text{PAH}}=0.038$) and PAH ionization fraction. The continuum spectrum of ISRF corresponding to each U value as a heating source of PAH and dust grains is not shown in Fig. 2(a) but included in the simulation of the observed spectrum (see Section 2.3). The PAH features and the continuum spectral shape are affected (i.e., weaker PAH emission and longer FIR peak wavelength) if one considers the attenuation of starlight incident on dust clouds.³⁸ For mMMP ISRF (used in this study) illuminating a foreground dust slab with $A_V = 2.0$, the PAH features are weakened by a factor of ~ 1.5 for $U = 10^3$ while the impact of attenuation on the PAH emission is negligible for the 3 Myr old ‘young’ starburst ISRF where the most of the stellar power is in the far-UV.³⁸ The difference in the PAH features between the attenuated and the unattenuated starlight is likely to be smaller for stronger ISRF (i.e., larger U) since the starlight from stronger ISRF can penetrate deeper. Since the model³⁸ computes the attenuated PAH spectra with a foreground dust slab for only one A_V value ($A_V = 2.0$), we cannot create the model PAH spectra for the ISRF with different dust attenuations. Also, the average strength of mMMP ISRF considered in the analysis (Section 3) is $U \sim 10^{3.5}$. Therefore, we expect that the effect of dust attenuation on the impinging starlight is small and adopt the model PAH emissivity

ⁱⁱⁱThe term ‘standard’ means the standard parameter values for grain size distribution function listed in Table 2 in Draine et al., 2021.³⁸



(a) Emissivity of PAH and dust grains



(b) Simulation of observed spectra

Fig 2 *Panel (a)*: Model emissivity of the mixture of PAHs and dust grains per H atom³⁸ for ‘standard’ grain size distribution, PAH ionization fraction, PAH mass fraction (q_{PAH}). The emissivity is computed based on a source of heating by the modified version of the starlight spectrum in the solar neighborhood³⁹ scaled up to 10^7 times larger than the value in the solar neighborhood. *Panel (b)*: Simulation of the observed spectrum from the model PAH and dust emissivity with $U = 10^4$ (Panel (a)) for a model galaxy with $L_{\text{IR}} = 10^{13.44} L_{\odot}$ and the chosen parameters of column density ($N_{\text{H}} = 10^{23} \text{cm}^{-2}$), size of the emitting region ($\ell = 2 \text{kpc}$), and luminosity distance (D_L). The PAH emissivity uses mMMP ISRF, a standard grain size distribution, and PAH ionization fraction, and $q_{\text{PAH}} = 0.038$. The thick gray dotted and the thick gray dashed line indicate a 5σ point source sensitivity (with 1-hour integration) of JWST/MIRI and PRIMA/FIRESS, respectively.

spectra from the unattenuated ISRF.

2.2 PRIMA FIRESS Sensitivity

The instrument parameters of the FIRESS base grating module³⁷ are given in Table 1. The nominal value of the point source sensitivity for an unresolved line (i.e., line sensitivity) with 5σ in 1-hour integration is $1.9 \times 10^{-19} \text{ W m}^{-2}$. The nominal 5σ point source continuum sensitivities in four observing bands for $R = 10$ binning in 1-hour integration, estimated from the PRIMA Exposure Time Calculator^{iv}, are also listed in Table 1. Using the spectral sampling (i.e., resolution) parameter for each band, we estimate the spectral sensitivity in units of Jy ($10^{-26} \text{ W m}^{-2} \text{ Hz}^{-1}$ or $10^{-23} \text{ erg s}^{-1} \text{ cm}^{-2} \text{ Hz}^{-1}$) as shown by the thick gray dashed line in Fig. 2(b).

Fig. 2(b) illustrates the observed mid-infrared (MIR) spectra of a galaxy at different redshifts by colored solid lines (see Section 2.3 for detailed prescription for computing the spectrum). For comparison, in Fig. 2(b), we also present a 5σ point source sensitivity with 1-hour integration for JWST/MIRI MRS (thick gray dotted line) scaled from the 10σ JWST/MIRI MRS sensitivity with 10,000 sec integration^v. The sensitivity of the MIRI MRS becomes poor with increasing wavelength and makes the use of Channel 4 ($> 18 \mu\text{m}$) very difficult for observing high-redshift PAH emission. In contrast, the PRIMA/FIRESS sensitivity (thick gray dashed line) for a point

^{iv} <https://prima.ipac.caltech.edu/page/etc-calc>

^v <https://jwst-docs.stsci.edu/jwst-mid-infrared-instrument/miri-performance/miri-sensitivity>

source is 1-2 orders of magnitude better than that of the long-wavelength channel of JWST/MIRI MRS and extends the redshift limit for observing PAH emissions to $z > 4$.

2.3 Observed PAH spectrum

The computation of the observed flux density at redshift z from the emissivity, νP_ν (erg s⁻¹ per H atom) requires gas column density ($N_{\text{H}}[\text{cm}^{-2}]$) and diameter of the emitting region (ℓ) as illustrated in Fig. 2(b). The spectral flux density, F_ν (Jy) is computed as

$$F_\nu = \frac{\pi}{4} \ell^2 N_{\text{H}} \frac{4\pi j_\nu}{n_{\text{H}}} \frac{1}{4\pi D_L^2} \quad (1)$$

where $j_\nu = \frac{1}{4\pi} P_\nu$ for isotropic emitter,⁴⁰ n_{H} is a volume density of hydrogen atom (H atom), and D_L is a luminosity distance at redshift z for a given cosmological model^{vi}. Although the line-of-sight dust extinction at V-band (A_V) is directly proportional to the gas column density (N_{H}), the dust attenuation due to a complex geometry of dust and stellar population is more complicated than the extinction and depends weakly on N_{H} .⁴¹ Also, we use the model spectra from unattenuated ISRF (Section 2.1). Therefore, we do not link the N_{H} to the attenuation of ISRF.

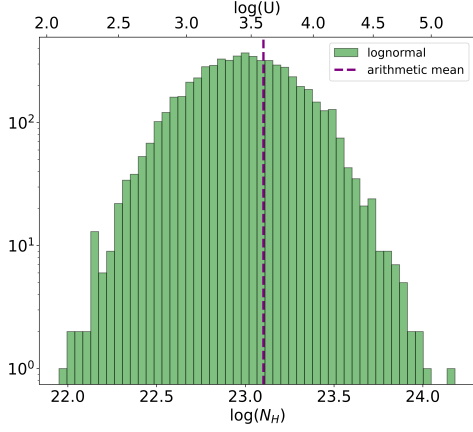
The term $\frac{4\pi j_\nu}{n_{\text{H}}}$ is given from the PAH-dust grain model³⁸ for the chosen parameters. In this study, we fix certain parameters: we use a modified version of the starlight spectrum in the solar neighborhood³⁹ called mMMP,³⁸ ‘standard’ grain size distribution and ‘standard’ PAH ionization fraction for computation (see Figure 9(a) and (b) in Draine et al., 2021³⁸). As discussed in Section 2.4 and 2.5, we adopt different values of the scale parameter of the strength of ISRF (U) relative to the value in the solar neighborhood³⁹ for a given column density and consider three different values of the mass fraction (relative to the total dust mass) of PAH molecules whose number of carbon atom is less than 1000, i.e., the parameter q_{PAH} .⁴²

Since the PAH model spectra³⁸ do not extend to the rest-frame optical and near-infrared (NIR) wavelengths, we combine the chosen ISRF energy density spectrum³⁸ (mMMP in this study) scaled by U and the PAH spectrum to construct the total spectrum. The total energy density spectrum of ISRF (erg cm⁻³), νu_ν is converted to a luminosity (erg s⁻¹) by integrating over the volume of a spherical shell^{vii} with a radius $\ell/2$ and a thickness c as light propagation distance per unit time and the luminosity is converted to the observed flux density for a given luminosity distance D_L at redshift z .

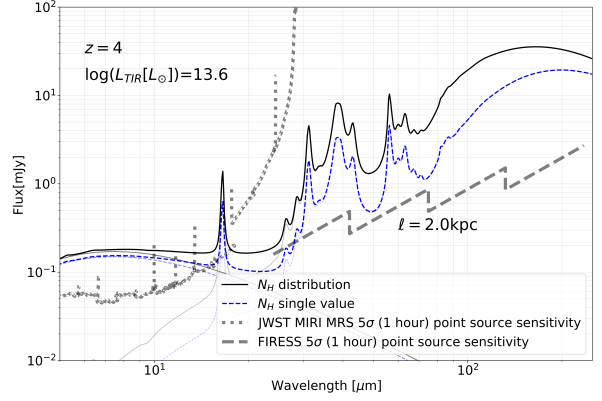
As an illustration, Fig. 2(b) shows the model spectrum of the dust and PAH molecules, including the ISRF spectrum for a galaxy observed at four different redshifts ($z = 2, 4, 6, 8$) represented by the solid lines with different colors. For each colored solid line, the thin gray dotted lines show ISRF spectra, and the thin solid gray lines show the PAH-dust spectra. Each spectrum is created using the same parameter value ($N_{\text{H}} = 10^{23} \text{cm}^{-2}$, $\ell = 2 \text{kpc}$, and $U = 10^4$). The total IR luminosity of the galaxy is obtained by scaling the total IR power (erg s⁻¹ per H atom) of each model spectrum model using the ISRF scale parameter U and converting it to the luminosity.

^{vi}In this study, we use the standard LCDM cosmological model with $H_0 = 70 \text{ km s}^{-1} \text{ Mpc}^{-1}$, $\Omega_m = 0.3$, $\Omega_\Lambda = 0.7$.

^{vii}Although the PAH spectrum is calculated based on a cylindrical geometry, a spherical geometry is used to calculate ISRF spectrum because a volume of spherical shell based on spherical geometry captures the ISRF distribution better than a volume of flat disk based on cylindrical geometry. For the same radius, the volume of a spherical shell is four times larger than that of a flat disk.

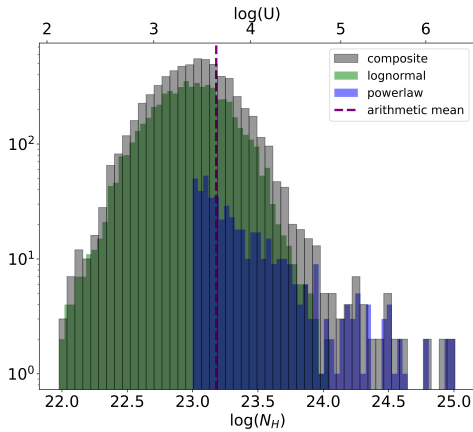


(a) Column density distribution

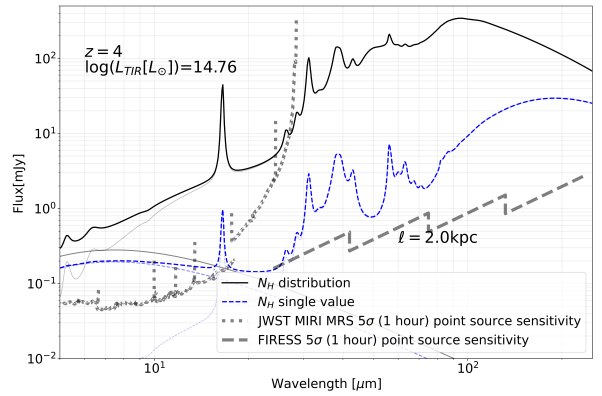


(b) Model spectra at $z = 4$

Fig 3 *Panel (a)*: Log-normal distribution of column density N_H with a variance $\sigma_s = 0.7$, sampled by 6000 random numbers centered at $\log(N_H[\text{cm}^{-2}]) = 23$. The purple vertical line indicates the arithmetic mean of N_H values. *Panel (b)*: Model PAH spectrum of a galaxy at $z = 4$ with $q_{\text{PAH}}=0.038$. The black solid line is obtained by ensemble averaging of the individual spectrum with the chosen N_H and associated U while the spectrum with the blue dashed line is obtained by the representative (i.e., arithmetic mean) value of N_H and U from the distribution.



(a) Column density distribution



(b) Model spectra at $z = 4$

Fig 4 Same as Fig. 3, but the column density distribution is a sum (shown by gray histogram) of log-normal (6000 random numbers shown by green histogram) and power-law distribution (using 500 random numbers shown by blue histogram) with a spectral slope of -2.5 .

2.4 Distributions of column density and ISRF

PRIMA with a 1.8m diameter mirror does not spatially resolve a high-redshift galaxy. The pixel sizes of the PRIMA/FIRESS are 7.6'' in Band 1/2, 12.7'' in Band 3, and 22.9'' in Band 4 (see Table 1), which implies that the observed PAH spectrum is a mixture of the contributions from many star-forming regions and diffuse ISM with different gas column densities and ISRF. Therefore, a PAH spectrum based on an ensemble of individual spectra from different regions is a more realistic model than a spectrum based on a single representative value for N_{H} and U .

It has been known that from observations and simulations, the column density probability distribution (N-PDF) is an important diagnostic of turbulence in local star-forming clouds^{43,44} and traces SFR.^{45,46} The two-component (lognormal and power law distribution) model of N-PDF is widely used to describe the observed N-PDF.^{47,48} A consensus is that the N-PDF of low column density gas and diffuse ISM follows a lognormal distribution while that of high column density gas and warm ISM follows a power law distribution.⁴⁷

The far-UV emission (FUV) is produced by OB associations so that the ISRF intensity will be proportional to the SFR surface density.⁴⁹ This relationship between ISRF and SFR surface density (Σ_{SFR}) can be refined and expressed as a function of inter-source opacity by considering a simple model of dust absorption in galactic disk.⁵⁰ If we use a tight correlation between Σ_{SFR} and gas surface density (Σ_{gas})² converted from N_{H} ($N_{\text{H}} \approx 10^{20} \text{cm}^{-2} \Sigma_{\text{gas}} / (1 \text{ M}_{\odot} \text{pc}^{-2})$ ⁵¹), we can parameterize the ISRF using N_{H} and Σ_{SFR} value at the solar neighborhood ($\Sigma_{\text{SFR},0}$) as follows.

$$U = \left[2.5 \times 10^{-4} \left(\frac{N_{\text{H}}}{10^{20} \text{cm}^{-2}} \right)^{1.4} \right] \times \frac{3}{\Sigma_{\text{SFR},0}} \quad (2)$$

where the factor 3 is chosen to be the value of the ratio between ISRF and Σ_{SFR} at the critical inter-source opacity.⁵⁰ We sample the distribution of N_{H} using lognormal (Fig. 3(a)) and lognormal with power law (Fig. 4(a)) distribution which also determines the ISRF scale factor U . Theoretical models of a turbulent ISM^{52,53} suggest that the variance of the lognormal distribution, σ_s , depends on the ISM Mach number ($\sigma_s^2 = \ln(1 + b\mathcal{M}^2)$ where \mathcal{M} is the ISM Mach number). For each random sample of N_{H} and U , we create a spectrum as explained in Section 2.3 by interpolating the spectrum in a grid of the U values. Then we average the ensemble of spectra created from each random sample of N_{H} and U with the assumption that the turbulent ISM only changes the distribution of N_{H} in the ISM and does not cause an effect on the PAH properties like grain size and ionization fraction. Here we note that the correlation between N_{H} and U may break at high column density because Σ_{SFR} reaches the Eddington limit (e.g., $\Sigma_{\text{SFR}} \approx 3000 \text{ M}_{\odot} \text{yr}^{-1} \text{kpc}^{-2}$ as a theoretical limit for starburst galaxies^{54,55}) and disrupts the surrounding gas. We verify that the required N_{H} to reach $\Sigma_{\text{SFR}} \approx 3000 \text{ M}_{\odot} \text{yr}^{-1} \text{kpc}^{-2}$ based on the KS relation² ($N_{\text{H}} = 1.48 \times 10^{25} \text{cm}^{-2}$) is lower than the maximum column density ($N_{\text{H}} = 10^{25} \text{cm}^{-2}$) sampled from lognormal distribution with high density power law tail (Fig. 4(a)). Also, we do not use the PAH spectra created from the lognormal+power law density distribution in our analysis (Section 3). Therefore, the simulations in this study based on the simple scaling relation (Equation 2) are performed for a physically reasonable parameter range.

A model spectrum of a galaxy at $z = 4$ computed based on a N_{H} density distribution following a lognormal distribution centered at $N_{\text{H}} = 10^{23} \text{cm}^{-2}$ with $\sigma_s = 0.7$ (Fig. 3(b)) has $\log(L_{\text{IR}}/L_{\odot}) = 13.6$. This value is similar to the observed (without lensing magnification correc-

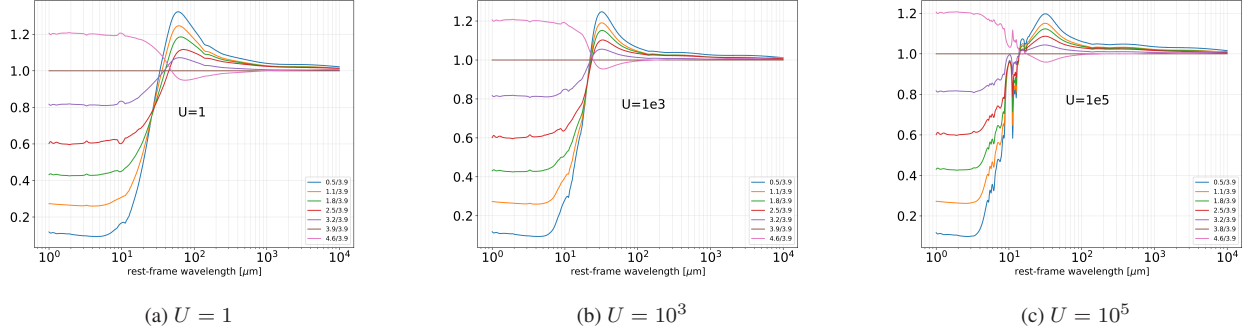


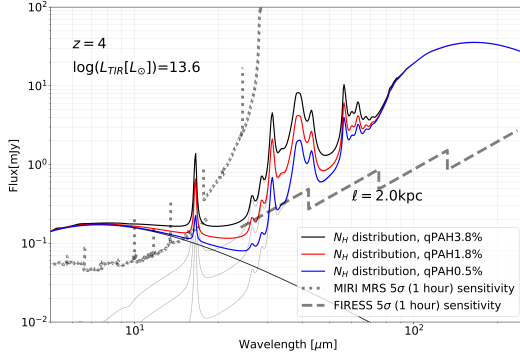
Fig 5 The PAH emissivity spectra with different q_{PAH} values (color lines) normalized by the reference spectrum computed with $q_{\text{PAH}} = 0.039$ for different ISRF scale parameter U using the model spectra⁴²

tion) L_{IR} value⁵⁶ ($\log(L_{\text{IR}}/L_{\odot}) = 13.9$) of a galaxy at $z = 4.22$ of which PAH emission was observed (3440 sec observing time) by JWST/MIRI MRS³⁵ and has a peak flux density (0.3 mJy) of the total (line and continuum) spectrum similar to the same model spectrum with lower q_{PAH} value (0.5%, see Fig. 6(a)). A model spectrum of the same galaxy with the same lognormal and an additional small fraction of power-law tail with a spectral slope of -2.5 (Fig. 4(b)) has much larger L_{IR} value ($\log(L_{\text{IR}}/L_{\odot}) = 14.76$) which is similar to the L_{IR} value of the most IR luminous galaxy W2246-0526⁵⁷ at $z = 4.6$ ($\log(L_{\text{IR}}/L_{\odot}) = 14.54$ ⁵⁸). The range of IR luminosity ($10^{12-15} L_{\odot}$) discussed in Section 3.1 and the L_{IR} value ($10^{13.6} L_{\odot}$) used for simulating the spectra presented in Section 3.2 are not far from reality: for example, high-redshift lensed dusty star-forming galaxies (PASSAGES⁵⁹) have intrinsic $L_{\text{IR}} \gtrsim 10^{13} L_{\odot}$ after magnification correction (median $\mu = 7$), implying much higher ‘apparent’ brightness.

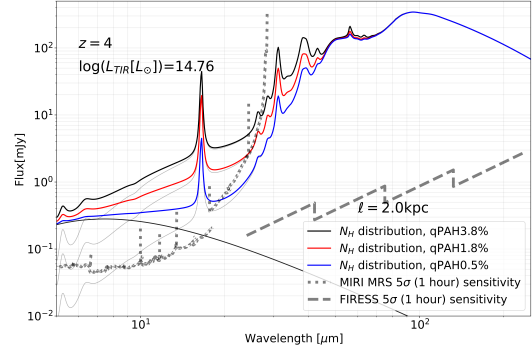
Remarkably, the spectrum with lognormal N_{H} distribution and additional small (8%) contribution from high-density regions following a power law N_{H} distribution (Fig. 4(b)) is very different from the one with the same lognormal N_{H} distribution only (Fig. 3(b)). Although the fraction is small, if there are regions with high Σ_{SFR} that are likely to have high U , the PAH emissivity for those high U regions (e.g., can be as large as $> 10\times$ the mean value as seen in Fig. 4(a)) is at least an order of magnitude larger (see Fig. 2(a)) and therefore contribution from the high U regions to the average spectrum becomes significant. This is an advantage for observing high-redshift galaxies with high Σ_{SFR} . The PAH spectrum with higher U also has a significantly different spectral shape from the one with lower U seen at $\approx 10\mu\text{m}$ silicate feature. Therefore a mixture of the spectra with low and high U might provide more flexibility to explain the observed ratio between different PAH bands.

2.5 Implementation of q_{PAH}

A deficit of the fraction of PAH luminosity relative to total dust continuum luminosity is found at low-metallicity environments.^{21,25,60–66} This PAH-metallicity relation (PZR)⁶⁶ implies that the inferred value of the mass fraction of PAH molecule with < 1000 carbon atoms (q_{PAH} parameter in the PAH model spectra⁴²) varies strongly with metallicity: lower q_{PAH} with decreasing metallicity.²⁵ Although the correlation between q_{PAH} and metallicity can be understood in a scenario where the hard radiation environment from high-mass stars in the low-metallicity ISM destroys preferentially the smallest grains,^{61,67} the observed correlation between PAH emission



(a) N_H distribution in Fig 3



(b) N_H distribution in Fig 4

Fig 6 Model spectrum in Fig.3(b) and 4(b) using N_H distribution (black solid line) and additional model spectra with the same parameters but different $qPAH$ values: red line for 1.8% and blue line for 0.5%

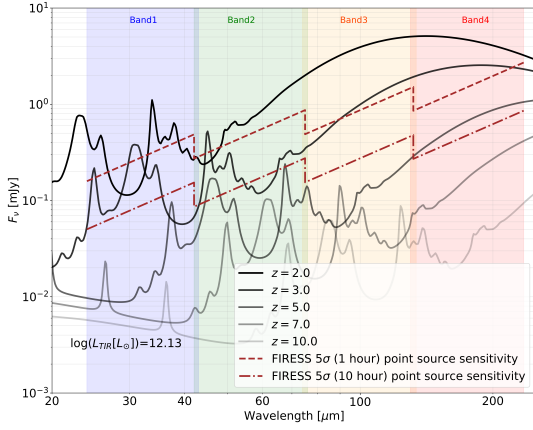
and metallicity are also affected by the efficiency of grain growth and the resulting dust grain size distribution.⁶⁶

Since galaxy gas metallicity has a clear trend with galaxy properties and redshift (lower mass galaxies at higher redshift tend to have lower metallicity⁶⁸), we explore three different (low, intermediate, and high) $qPAH$ values: 0.5, 1.8, 3.8% of which corresponding metallicities from the PZR relation⁶⁶ are 0.2, 0.5, $0.8Z_\odot$ respectively. The PAH model in this study using standard grain size distribution³⁸ has the spectra computed for $qPAH=0.038$ only, which does not allow us to derive the model spectra with lower $qPAH$ values. Thus we use the previous model⁴² that computes the PAH spectra with varying $qPAH$ value for the nearly same ISRF (MMP³⁹) as the one in the current model and calculate the ratio between the spectrum with varying $qPAH$ values relative to the reference spectrum with $qPAH=0.039$ ^{viii}. This ratio is applied to our model spectra (computed with $qPAH=0.038$ with standard grain size distribution).

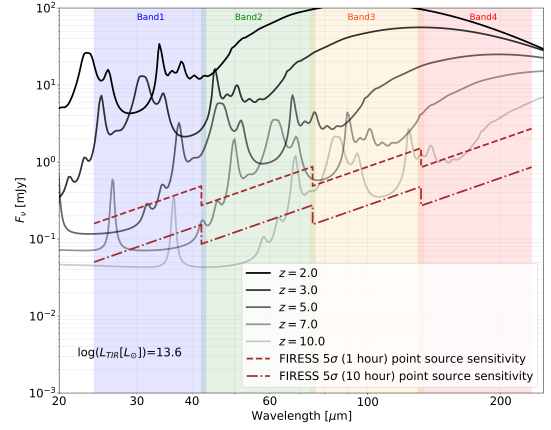
Fig. 5 presents the examples of PAH emissivity spectra with different $qPAH$ values normalized by the reference spectrum with $qPAH=0.039$ computed using the model spectra.⁴² Three panels in Fig. 5 show the case with low ($U=1$), intermediate ($U=10^3$), and high ($U=10^5$) U parameters. The PAH emissivity spectra normalized by the reference spectrum with $qPAH=0.039$ have different shapes for different U values. For simplicity, we do not assign $qPAH$ for each sampled spectrum with N_H value and globally apply the same $qPAH$ value for the entire region of the galaxy. For a given N_H sample distribution with the corresponding average U value, we estimate the normalized PAH emissivity spectra to the reference spectrum (like the ones in Fig. 5) by interpolating the two normalized PAH emissivity spectra of which U values from the model grid are bracketing the average U value from the given N_H distribution. Then the normalization of the PAH emissivity for two chosen $qPAH$ values (0.005 and 0.018 in Fig. 5) are applied to the model spectrum computed with $qPAH=0.038$ to create two additional model spectra for low and intermediate $qPAH$ values.

Fig. 6 shows the model spectra with three different $qPAH$ values ($qPAH=0.005, 0.018, 0.038$). The model spectrum with $qPAH=0.038$ (black solid line) in Panel (a) and (b) are the same model

^{viii}We note that the model with varying $qPAH$ ⁴² value does not have the spectra with the exact $qPAH(0.038)$ used in this study, however, the difference should be negligible.



(a) lognormal: $\bar{N}_H = 2.5 \times 10^{22} \text{cm}^{-2}$



(b) lognormal: $\bar{N}_H = 1 \times 10^{23} \text{cm}^{-2}$

Fig 7 Model spectrum of the PAH bands in the PRIMA/FIRESS observing bands at $z = 2, 3, 5, 7, 10$. The spectrum is computed from three different lognormal distributions with the same variance ($\sigma_s = 0.7$) and different means. $q_{\text{PAH}} = 0.038$ is used for all spectra. The purple dashed line and the purple dot-dashed line indicate a 5σ sensitivity of the PRIMA/FIRESS from 1-hour and 10-hour integration, respectively.

spectrum in Fig. 3 and Fig. 4, respectively. In Panel (a) and (b), two additional spectra with low and intermediate q_{PAH} value (blue and red solid lines) are shown. As expected, the resulting spectrum with lower q_{PAH} value has weaker PAH emission in both line and continuum.

2.6 Simulation of the PRIMA/FIRESS spectrum with noise realization

For investigating the science case of the PRIMA/FIRESS to observe PAH emission spectrum from high-redshift galaxies, we simulate the noise-added spectrum with the spectral channel width specified in Table 1. A 1σ Gaussian noise based on the 5σ point source sensitivity curve with 1-hour integration (thick gray dashed lines in Fig. 2(b)) is added to the noiseless model spectrum. Additionally, we convolve the model spectrum with the PRIMA/FIRESS spectral response function (i.e., Gaussian with a finite FWHM^{ix} from Bradford et al. (this volume)) to consider a proper instrumental effect. Here we assume that the noise due to the PRIMA/FIRESS point source sensitivity is larger than a systematic noise due to the effect of slit width (less significant for a point source) and the background flux confusion noise primarily due to PRIMA's small (1.8m) mirror diameter is less significant for the FIRESS spectroscopy because of an additional velocity dimension as discussed in the conceptual study of the previous FIR spectrometer mission, Origins Space Telescope.⁶⁹ All synthetic spectra (Fig. 8) presented in Section 3.2 are the simulations of PAH emission from a model galaxy with $\log(L_{\text{IR}}/L_{\odot}) = 13.6$ (Fig. 7(b)) observed by PRIMA/FIRESS with 1-hour integration.

^{ix}FWHM for the spectral response function is specified per spectral channel with very small difference between adjacent channels. However, for simplicity, we use a single averaged value for each band: 0.186, 0.427, 0.761, and $1.32\mu\text{m}$ for Band 1, 2, 3, and 4, respectively.

3 Result

This study characterizes the capability of the FIRESS low-resolution spectroscopy for detecting PAH emission from high-redshift galaxies and for measuring the luminosity of PAH bands. Following the methods described in Section 2, we simulate the spectra composed of PAHs, dust, and stellar radiation observed by PRIMA/FIRESS for a 1-hour long integration. Although the lognormal column density distribution with a power law tail produces a significantly brighter spectrum than the one from the lognormal distribution, for a conservative result, we choose a lognormal N_{H} distribution. Before we present the result, we note two important assumptions in this investigation.

First, we use a point source sensitivity of the PRIMA/FIRESS in this investigation, which implies that the sources are not spatially resolved. The pixel size of the PRIMA/FIRESS specified in Table 1 ranges from $7.6''$ in Band 1 to $22.9''$ in Band 4. Therefore, the adopted point source sensitivity works ideally for isolated high-redshift galaxies without close neighbors within 70–140 kpc distance at $z = 2 \sim 4$. However, for spatially blended sources, the redshift information from spectroscopic observation may help alleviate the spatial confusion as discussed in Section 2.6. Second, we assume an emitting region with 2 kpc diameter ($\ell = 2\text{kpc}$) when creating an ensemble-averaged spectrum. We chose 2 kpc diameter (or 1 kpc radius) because the redshift evolution of galaxy size based on a large ($\sim 190,000$) sample of galaxies after morphological K -correction suggests that the effective radii of galaxies at $z = 0–6$ are approximately 1 kpc.⁷⁰ However, recent observations suggest that the effective radii of galaxies at very high-redshift ($z \sim 10$) discovered by JWST are typically a few 100 pc,⁷¹ although the stellar mass and size relation from a small number of samples at such high-redshift is not well characterized yet.

If an effective radius of 300 pc is assumed for dust in galaxies at $z \gtrsim 7$, one can infer from Equation 1 that the overall brightness of the simulated spectra decreases by a factor of 10 and the required integration time for detection with the same 5σ significance becomes 100 hours. However, we note that even under this assumption (i.e., 300 pc effective radius), the peak flux density of the PAH emission bands at 6.2 , 7.7 , and $11.2\mu\text{m}$ for IR bright galaxy at $z = 7$ ($\log(L_{\text{IR}}/L_{\odot}) = 13.6$ shown in Fig. 7(b)) are larger than 5σ sensitivity with 10-hour integration and small galaxies at the end of reionization can be detected by PRIMA/FIRESS with modest observing time ($\gtrsim 10$ hours).

3.1 PRIMA FIRESS observing bands and sensitivities for PAH detection

We simulate the noiseless PAH spectra observable with the FIRESS observing bands in different redshifts and compare them with the 5σ sensitivities. Fig. 7 shows the simulated PAH spectra with $q_{\text{PAH}} = 0.038$ at $z = 2, 3, 5, 7, 10$ for two different lognormal N_{H} distributions that have the same variance but different means (Panel (a) and (b)). The purple dashed line and purple dot-dashed line indicate 5σ point source sensitivity from 1-hour and 10-hour integration, respectively. As described in Section 2.4, a chosen lognormal distribution determines the distribution of U and the total IR luminosity (annotated in each panel).

First, one can see that $7.7\mu\text{m}$ PAH emission band moves into the observing window of Band 1 for redshift $z = 2 \sim 3$ (cosmic noon), Band 2 for redshift $z = 5 \sim 7$ (epoch of reionization), and Band 3 for redshift $z > 7$ (cosmic dawn). Second, most PAH bands are observable up to $z \sim 7$ for a spectrum based on a lognormal distribution with $\bar{N}_{\text{H}} \geq 1 \times 10^{23}\text{cm}^{-2}$ ($\log(L_{\text{IR}}/L_{\odot}) \gtrsim 13.6$) although the significance of the observation is weak if q_{PAH} is smaller. Third, as shown in Panel(a) for $\log(L_{\text{IR}}/L_{\odot}) = 12.13$, the peak of the 6.2 , 7.7 , and $11.2\mu\text{m}$ band PAH emission is above a 5σ sensitivity at $z = 3$ and $7.7\mu\text{m}$ band PAH emission is above a 2.8σ sensitivity even at

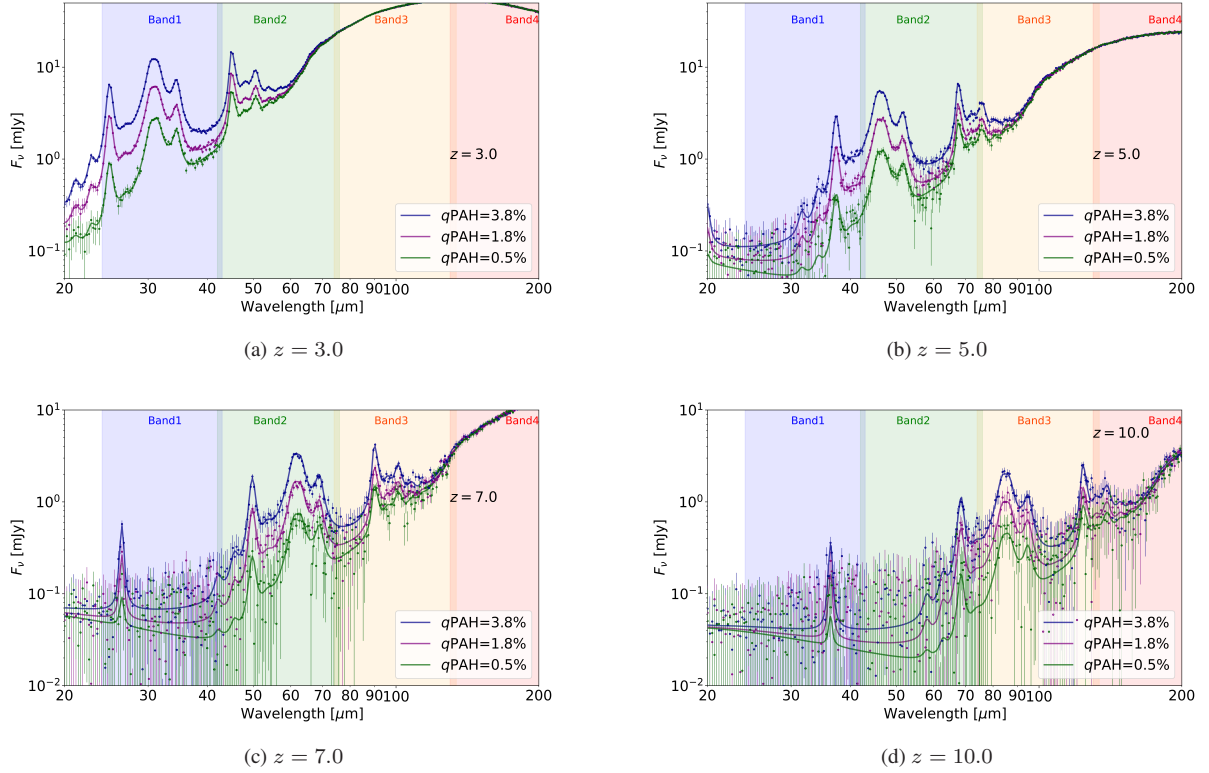


Fig 8 Simulated PRIMA/FIRESS spectrum of the PAH emission based on the model spectrum for a galaxy with $\log(L_{\text{IR}}/L_{\odot}) = 13.6$ in Fig. 7(b) for selective redshifts ($z = 3, 5, 7, 10$). In addition to $q\text{PAH} = 0.038$, two lower $q\text{PAH}$ values (1.8 and 0.5%) are used for simulation. Dark blue, purple, and green solid lines represent the noiseless model spectrum with $q\text{PAH} = 0.038, 0.018, 0.005$ respectively.

$z = 5$, after 1-hour integration, which is more than an order of magnitude smaller than the VLA observing time ($10 \sim 70$ hours as shown in Fig. 1(c)) for the CO(1-0) brightness for the similar L_{IR} ($\log(L_{\text{IR}}/L_{\odot}) \sim 12$).

Although the methods of flux measurement and the $q\text{PAH}$ value may change the significance of detection, the PRIMA/FIRESS with the current instrument specification (Table 1) is capable of observing PAH emission over a wide range of redshift: from cosmic noon to cosmic dawn if a PAH emitting galaxy is extremely IR bright (HyLIRGs or lensed star-burst galaxies with $L_{\text{IR}} \gtrsim 10^{13} L_{\odot}$) and has a dense ($\bar{N}_{\text{H}} \sim 1 \times 10^{23} \text{cm}^{-2}$) ISM. If the integration time increases to 10 hours (i.e., $3.3 \times$ more sensitive than 1-hour integration), the galaxy L_{IR} limit to detect PAH emissions becomes lower and the ULIRGs-like ($L_{\text{IR}} \gtrsim 10^{12} L_{\odot}$) objects can be detectable in $7.7 \mu\text{m}$ PAH band up to the end of cosmic reionization epoch ($z \sim 5$) as seen in Fig. 7(a).

3.2 PAH flux measurement from PRIMA/FIRESS spectra

In Fig. 8, we show the noise-added spectra (explained in Section 2.6) for a galaxy observed at $z = 3, 5, 7, 10$ simulated from the noiseless model spectra in Fig. 7(b) with the spectral channel width and sensitivity specified in Table 1. In each panel, the three spectra represent the simulation with high, intermediate, and low $q\text{PAH}$ values (explained in Section 2.5) shown by dark blue

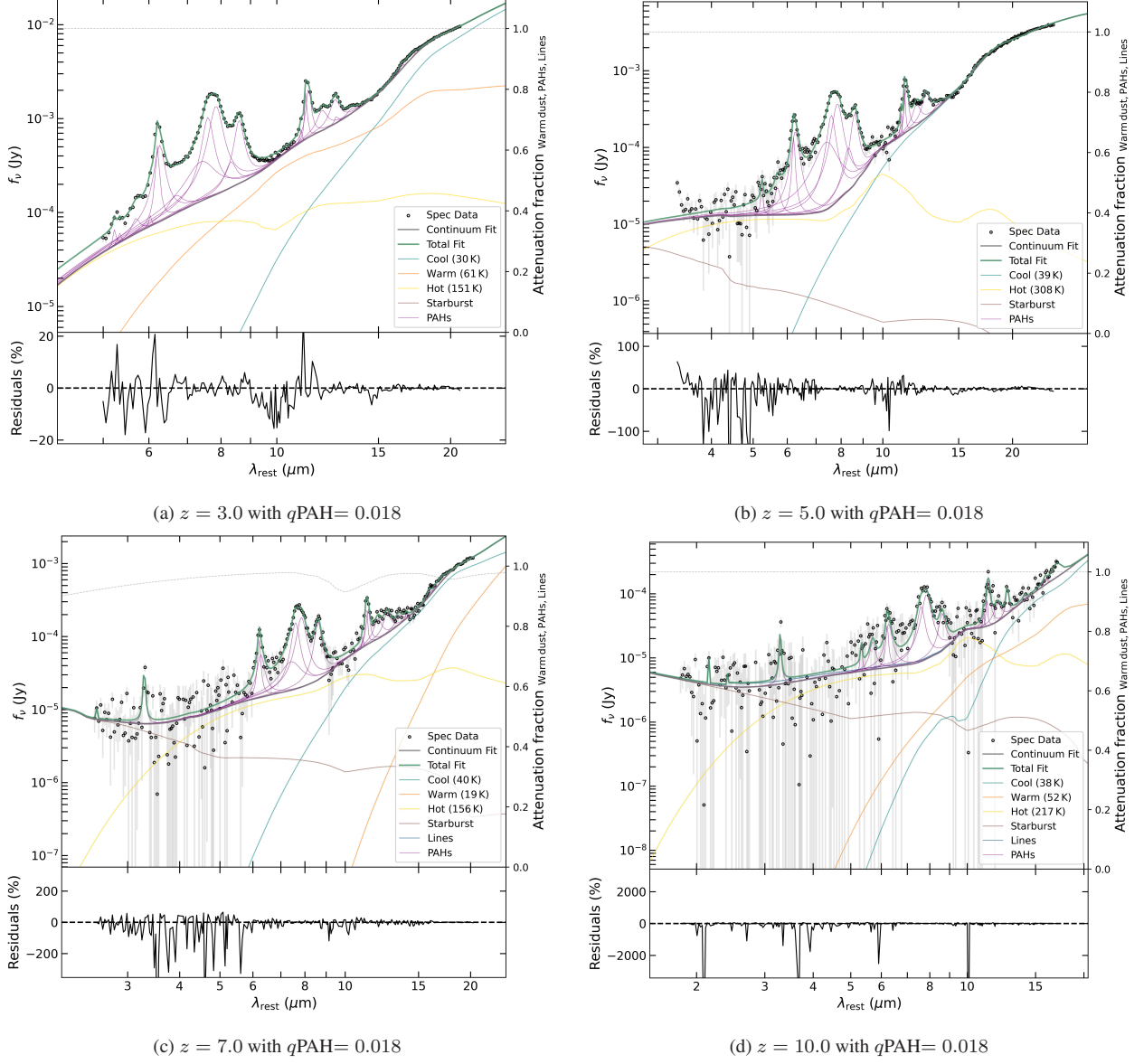


Fig 9 Full spectral modeling of the PAH spectrum using CAFE. The spectral data (black circle) with gray error bars in each panel for different redshifts is the simulated PAH spectrum with $q_{\text{PAH}} = 0.018$ in the corresponding panel in Fig. 8. The attenuation of the model PAH emission (gray dashed line showing attenuation fraction of 1.0) is negligible except for Panel (c) showing a mild variation of the attenuation (10% at maximum).

(3.8%), purple (1.8%), and green (0.5%) colors. The spectrum becomes noisy due to decreasing flux density with increasing redshift. To measure the flux density in the PAH emission bands in Fig. 8, we use the PAH spectral modeling tool, CAFE^x that was originally developed for fitting Spitzer/IRS spectra and later updated to work with JWST IFU data.

Fig. 9 shows the result of the CAFE model fitting to the spectral data. Each panel shows the spectrum for intermediate $q\text{PAH}$ value ($q\text{PAH} = 0.018$) and the best-fit CAFE model, with the residual spectrum in the bottom panel. The input parameter file for starburst galaxies is used for modeling the PAH spectrum for all four cases. In each panel, multiple PAH complexes are shown in purple lines with additional baseline emissions including emissions from cool, warm, and hot dust components, some of which may be degenerate (e.g., warm and cool dust temperatures are swapped as seen in Fig. 9(c)). The attenuation of the model PAH emissions (gray dashed line in each panel showing the attenuation fraction) for fitting the spectra is negligible (attenuation fraction: 1.0) except for the mild variation of attenuation ($< 10\%$) seen in Fig. 9(c). The fits are successful with reasonable residuals: the difference between the data and the best-fit model for the largest deviant data point is $\pm 20\%$ for $z = 3$ and $\pm 100\%$ for $z = 5$ (due to the data points with low signal-to-noise ratio) without a significant systematic bias. Even for lower signal-to-noise ratio spectra at higher redshift ($z = 7, 10$), the CAFE produces a robust fit to the 6.2 and $7.7\mu\text{m}$ features. In particular, even though the $3.3\mu\text{m}$ features are noisy at high redshift ($z \gtrsim 7$), the spectral fitting robustly captures the 6.2 , 7.7 , and $11.2\mu\text{m}$ features (Fig. 9(c) and (d)), which shows a promise for the use of the 6.2 and $7.7\mu\text{m}$ feature to detect high-redshift galaxies.

We also note that, since the PAH emission spectral features are broad, the high-redshift PAH emission spectrum observed in a single FIRESS band may not have sufficient continuum baseline to determine the PAH flux density accurately. For example, Fig. 8(a) shows that the FIRESS band 1 does not fully cover 6.2 and $7.7\mu\text{m}$ PAH emission from a $z = 3.0$ galaxy. Likewise, Fig. 8(b) shows that the FIRESS band 2 does not fully cover 7.7 and $11.2\mu\text{m}$ PAH emission from a $z = 5.0$ galaxy. The limited continuum baseline from a single band observation may introduce a bias in the PAH luminosity measurement from spectral fitting or may not even allow a simple measurement based on a flux ‘clip’ using a pre-fixed frequency range.³⁸ For example, we find that the model PAH luminosities at 7.7 and $11.2\mu\text{m}$ from CAFE using the spectra from all four bands and from only Band 2 for a $z = 5.0$ galaxy (Fig. 8(b)) differ by 4% for the $7.7\mu\text{m}$ PAH and 15% for the $11.2\mu\text{m}$ PAH. Given that the redshifted PAH emission spectrum may cross the edges of the FIRESS bands, the best practice for observing high-redshift PAH emission using PRIMA/FIRESS is probably to use at least two bands, or all bands if possible.

3.3 Full spectral modeling and ‘clip’ methods

If a single band is used for observation without a sufficient continuum baseline for spectral fitting, one can measure the flux density by integrating the spectrum over a certain frequency range that was originally introduced as ‘clip’ methods.³⁸ If one assumes that the physically motivated spectral modeling measures the true luminosities of PAH emission, it is useful to check how close this simple ‘clipped’ flux is to the one obtained by spectral fitting.

Compared to the full spectral modeling, the flux measured by ‘clip’ methods is expected to be small. However, if the difference between the ‘clipped’ flux and the spectral model flux is just a constant offset and does not depend on the physical conditions of the PAH grains and ISM, the

^x <https://github.com/GOALS-survey/CAFE>

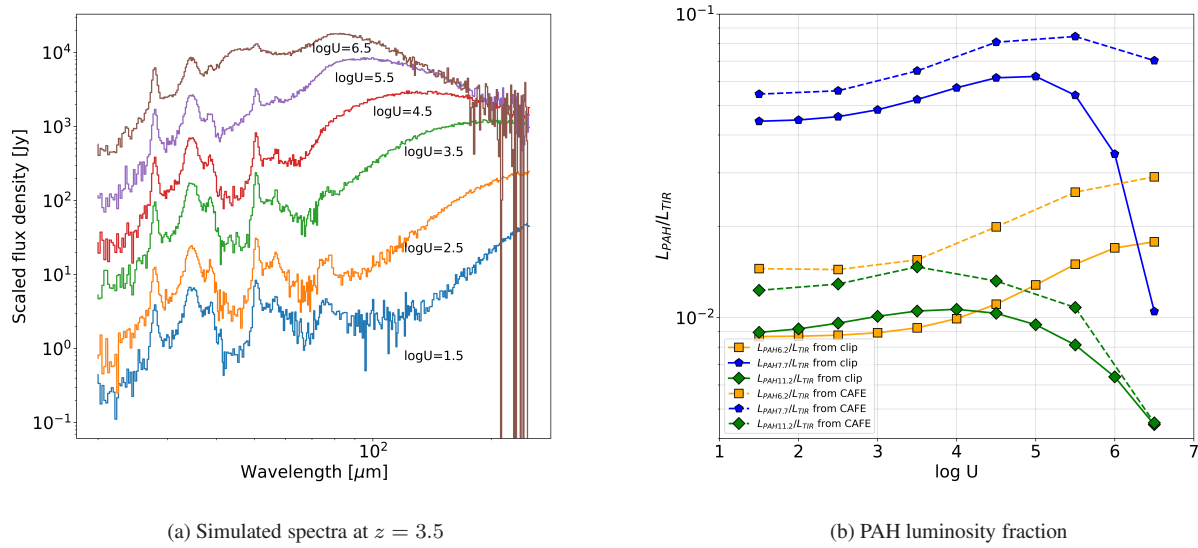


Fig 10 Two different measures of the PAH luminosity (full spectral modeling and ‘clip’ method³⁸) at 6.2, 7.7, and 11.2 μm are compared. *Panel(a)*: simulated noised added spectra at $z = 3.5$ from the model PAH emissivity for given U are shown. The spectra are scaled such that they all have a similar signal-to-noise ratio. *Panel(b)*: fractional luminosity of the PAH emission relative to L_{IR} are shown as a function of the ISRF scaling parameter, U . The symbols connected by solid lines are obtained by measuring the flux density of the ‘noise-less’ model spectrum using the ‘clip’ method while the symbols connected by dashed lines are obtained by measuring the PAH emission from the spectra in Panel(a) using full spectral modeling tool CAFE.

‘clip’ method is a simple and useful way of understanding the physics of PAH emission (grain size, ionization, ISRF) as often characterized by the PAH band ratios.³⁸

Fig. 10(a) shows the simulated noise-added spectra based on the model PAH emissivity (see Fig. 2(a)) for different U values. The spectra being set to have a similar signal-to-noise ratio are shown with an arbitrary amplitude scale to present them well-separated in Fig. 10(a) for clear visibility. Fig. 10(b) shows the fractional luminosity to the total IR luminosity for the PAH emissions at 6.2, 7.7, and 11.2 μm bands as a function of U . The symbols connected by the solid lines represent the value estimated from ‘clip’ methods based on the noiseless model spectra³⁸ for given U . The same symbols connected by the dashed line represent the value determined by the model PAH emission component from the CAFE spectral modeling of the noise-added simulated spectrum for selective values of U (Panel(a)). For a fair comparison to the ‘clip’ methods which cannot estimate the attenuation corrected intrinsic flux value, we used the value uncorrected for attenuation (i.e., the observed value) from the CAFE model, although the attenuation fractions required for fitting were indeed negligible.^{xi} The same input parameter file for starburst is used for all spectra for the CAFE model except for the spectrum with the highest U value ($\log U = 6.5$) for which we have to use the input parameter file for AGN because the cool component of dust grains does not produce a

^{xi}The attenuation model of PAH spectra based on the 9.7 μm silicate dust optical depth $\tau_{9.7}$ suggests a systematic change of the PAH band ratio as a function of $\tau_{9.7}$.⁷² However, given the relation between A_V and $\tau_{9.7}$ ($A_V/\tau_{9.7} = 18.5$) for diffuse Galactic dust,⁷³ we note that the A_V value inferred from N_H value⁷⁴ ($N_H/A_V = 1.9 \times 10^{21} \text{cm}^{-2} \text{mag}^{-1}$ for $R_V = 3.1$) used in this study results in $\tau_{9.7} \approx 1$ causing a relatively small impact.

good fit for both the continuum flux presented shortward of $3.3\mu\text{m}$ PAH feature and a characteristic ‘AGN-dominated’ MIR feature.⁷⁵

With increasing U , a significant change in the spectral shape is noticeable at the $\approx 10\mu\text{m}$ silicate feature between 7.7 and $11.2\mu\text{m}$ PAH features (Fig. 10(a)). As a result, the spectral fitting with different shapes of continuum emission alters the contribution from PAH emission which may result in a significantly different value from the simple estimate based on ‘clip’ methods. In Fig. 10(b), we can see that the fractional luminosity of PAH emission for 7.7 (blue color) and $11.2\mu\text{m}$ (green color) measured from the spectral fitting and ‘clip’ methods are in parallel with a constant offset for low U ($\log U < 4$) and then become different from each other for high U ($\log U \gtrsim 4$) when strong ISRF significantly alters the spectral shape of the model PAH emissivity. Unlike the 7.7 and $11.2\mu\text{m}$ PAH bands close to the $9.7\mu\text{m}$ silicate feature, the $6.2\mu\text{m}$ PAH emission (yellow color) shows the same trend of the fractional luminosity as a function of U for the estimate from both spectral fitting and ‘clip’ methods.

4 Synergy with Fast Mapping Speed

In this paper, the focus of our investigation is the capability of PRIMA/FIRESS to observe the PAH emissions from high-redshift galaxies using a pointing mode observation. However, PRIMA is also efficient in mapping. The time to survey 100 arcmin^2 area for 5σ line sensitivity, $3 \times 10^{-19} \text{ W m}^{-2}$, is 800 hours for $23\text{--}75\mu\text{m}$ (Band 1 and 2) and $336 \text{ hours} \times (\lambda/100\mu\text{m})^{-1.68}$ for $75\text{--}235\mu\text{m}$ (Band 3 and 4).³⁷ This is more than $10\times$ faster than JWST/MIRI and Spitzer/IRS at the similar observing wavelength.³⁷ The nominal sensitivity for pointing observation used in this study ($1.9 \times 10^{-19} \text{ W m}^{-2}$) is comparable to this mapping sensitivity and therefore our findings on the capability of PRIMA/FIRESS for detecting PAH emission from high-redshift galaxies also hold for PAH mapping (with 63% degraded sensitivity for the same observing parameters and physical properties of galaxies). One should note that this synergy between the high sensitivity for PAH detection and the fast mapping speed makes PRIMA/FIRESS an efficient instrument for PAH mapping. Here we discuss galaxy protocluster as an example science case for PAH mapping.

High-redshift protoclusters are important tracers of the structure formation in the early Universe. However, it is difficult to spectroscopically confirm the membership of each galaxy in the protocluster due to the large sky area and the faint line emission. If the PAH emission is bright, one can use PRIMA/FIRESS to map the high-redshift galaxy protoclusters with a typical angular size of a few arcmin at $z = 2$,⁷⁶ which will detect PAH emissions from individual galaxies with sufficient SFR ($\text{SFR} = 100 \sim 1000 \text{ M}_\odot \text{yr}^{-1}$ based on the $\text{SFR}-L_{\text{IR}}$ correlation,⁷⁷ $\text{SFR} = 10^{-10} (L_{\text{IR}}/L_\odot) \text{ M}_\odot \text{yr}^{-1}$) and confirm their redshift. If we use the measured overdensities of the galaxies in protoclusters at $z = 2 \sim 3$ and count their spectroscopically confirmed member galaxies,⁷⁸ the estimated number density of the protocluster member galaxies is ≈ 4 per arcmin^2 (i.e., $\approx 20''$ distance to the closest neighbor for each member galaxy). With $7.6''$ pixel size for Band 1 of the PRIMA/FIRESS in which the observed PAH emissions from galaxies at $z = 2 \sim 3$ are detectable, the PRIMA/FIRESS is capable of observing individual member galaxies without a significant impact of the blended sources in the pixel.

For a galaxy protocluster at cosmic noon ($z = 2 \sim 3$) traced by enhanced number of submillimeter galaxies with $\text{SFR} = 100 \sim 1000 \text{ M}_\odot \text{yr}^{-1}$, the PRIMA/FIRESS Band 1 can map the entire protocluster and detect PAH emission from its member galaxies (see Fig. 7) with $\lesssim 100$ hours. The membership confirmation will be more reliable by full spectroscopic mapping, for

example, using FIRESS Band 1 and 2 to detect multiple PAH emission lines as shown in Fig. 8(a). PRIMA/FIRESS mapping is much more efficient than observing CO from a handful of selected member galaxies at $z \sim 3$ with ≈ 30 hours of VLA time for each galaxy (Fig. 1(c)).

5 Summary

In this paper, we perform a simulation of the observed PAH spectra of spatially unresolved high-redshift galaxies for PRIMA/FIRESS with low-resolution ($R \sim 100$) spectroscopy. The model PAH emissivity spectrum is converted to the observed spectrum at a given redshift with the FIRESS channel resolution, using cylindrical geometry with column density distribution and “low,” “intermediate,” and “high” q_{PAH} values. Random Gaussian noise added to the spectra is created based on the PRIMA/FIRESS sensitivity and the PRIMA/FIRESS spectral response function is convolved with the model spectra. The principal results of this study are as follows.

1. We calculate the observed PAH spectra based on an ensemble distribution of gas column density following the form of lognormal and lognormal with a power-law tail. The addition of a small fraction of power-law tail that represents high-density star-forming regions with strong ISRF, changes the shape of the averaged spectrum and increases its brightness.
2. The bright $7.7\mu\text{m}$ PAH emission band is shifted to the PRIMA/FIRESS Band 1 window for $z = 2 \sim 3$, Band 2 window for $z = 5 \sim 7$, and Band 3 window for $z > 7$. For 1 hour integration, most of the well-known PAH bands ($3.3, 6.2, 7.7, 11.2\mu\text{m}$) are observable at $z \sim 7$ for a galaxy with $L_{\text{IR}} \sim 1 \times 10^{13} L_{\odot}$. For 10 hour integration, the $7.7\mu\text{m}$ PAH band is observable at $z \sim 5$ for a galaxy with $L_{\text{IR}} \sim 1 \times 10^{12} L_{\odot}$. The required observing time for detecting PAH emission is an order of magnitude lower than the VLA observing time for CO(1-0) observation of a galaxy with a similar L_{IR} .
3. We simulate the measurement of the PAH emission by modeling the synthetic spectra using physically motivated near- and mid-IR spectral modeling tool, CAFE. For a range of redshifts ($z = 3, 5, 7, 10$), the CAFE fits the synthetic spectra and produces robust fitting results: for the data point with the largest deviation from the best-fit model, $\pm 20\%$ residual for $z = 3$ and $\pm 100\%$ residual for $z = 5$ (due to the data points with the lowest signal-to-noise ratio) without a significant systematic bias. Even for lower signal-to-noise ratio spectra at higher redshift ($z = 7, 10$), the CAFE produces a robust fitting to the 6.2 and $7.7\mu\text{m}$ features. For reliable spectral modeling of the broad PAH emission feature, which may cross the edge of the FIRESS band, the best practice is to use at least two bands for observation.
4. We compare the measurement of the PAH luminosity from a simple ‘clip’ method based on a pre-fixed frequency range and from spectral fitting methods. For weak ISRF strength ($\log U < 4$), the fractional luminosities of PAH emissions relative to the total IR luminosity as a function of U shows the same trend for $6.2, 7.7, 11.2\mu\text{m}$, however with increasing ISRF intensity ($\log U \gtrsim 4$), the measurements from the two methods do not show the same trend: the difference is significant in the 7.7 and $11.2\mu\text{m}$ features while the $6.2\mu\text{m}$ feature still shows the same trend for the measurement from both methods.
5. PRIMA/FIRESS can be used as a mapping instrument to measure star formation and redshift of the member galaxies in the entire region of a galaxy protocluster at $z = 2 - 3$ by observing bright PAH emissions.

Our study suggests that PRIMA/FIRESS low-resolution spectroscopy has promise for observing PAH emissions from high-redshift galaxies. The specification of the FIRESS instrument complements the long-wavelength channels of the JWST/MIRI MRS with 1-2 orders of magnitude better sensitivity. Thus, PRIMA/FIRESS can extend PAH observation to higher redshifts ($z > 4$) where the spectroscopic observation of PAH using JWST/MIRI MRS is practically infeasible.

Code and Data Availability

The code used to generate the results and figures is available in the following Github repository. Data sharing is not applicable to this article, as no new data were created or analyzed.

https://github.com/ilsangyoon/PRIMA_FIRESS.git

Disclosure

The authors declare that there are no financial interests, commercial affiliations, or other potential conflicts of interest that could have influenced the objectivity of this research or the writing of this paper.

Acknowledgments

The authors thank two anonymous referees for their constructive comments which improved the paper. The National Radio Astronomy Observatory is a facility of the U.S. National Science Foundation operated under cooperative agreement by Associated Universities, Inc. This research was carried out in part at the Jet Propulsion Laboratory, California Institute of Technology, under a contract with the National Aeronautics and Space Administration. I.S. acknowledges fundings from the European Research Council (ERC) DistantDust (Grant No.101117541) and the Atracción de Talento Grant No.2022-T1/TIC-20472 of the Comunidad de Madrid, Spain. IGB is supported by the Programa Atracción de Talento Investigador “César Nombela” via grant 2023-T1/TEC-29030 funded by the Community of Madrid.

References

- 1 P. Madau and M. Dickinson, “Cosmic Star-Formation History,” *ARA&A* **52**, 415–486 (2014).
- 2 R. C. Kennicutt, Jr., “The Global Schmidt Law in Star-forming Galaxies,” *ApJ* **498**, 541–552 (1998).
- 3 A. K. Leroy, A. Bolatto, K. Gordon, *et al.*, “The CO-to-H₂ Conversion Factor from Infrared Dust Emission across the Local Group,” *ApJ* **737**, 12 (2011).
- 4 F. Bigiel, A. K. Leroy, F. Walter, *et al.*, “A Constant Molecular Gas Depletion Time in Nearby Disk Galaxies,” *ApJL* **730**, L13 (2011).
- 5 A. Schruba, A. K. Leroy, F. Walter, *et al.*, “Low CO Luminosities in Dwarf Galaxies,” *AJ* **143**, 138 (2012).
- 6 C. L. Carilli and F. Walter, “Cool Gas in High-Redshift Galaxies,” *ARA&A* **51**, 105–161 (2013).
- 7 E. Daddi, F. Bournaud, F. Walter, *et al.*, “Very High Gas Fractions and Extended Gas Reservoirs in $z = 1.5$ Disk Galaxies,” *ApJ* **713**, 686–707 (2010).
- 8 E. Daddi, H. Dannerbauer, D. Liu, *et al.*, “CO excitation of normal star-forming galaxies out to $z = 1.5$ as regulated by the properties of their interstellar medium,” *A&A* **577**, A46 (2015).

- 9 L. J. Tacconi, R. Genzel, R. Neri, *et al.*, “High molecular gas fractions in normal massive star-forming galaxies in the young Universe,” *Nature* **463**, 781–784 (2010).
- 10 L. J. Tacconi, R. Genzel, A. Saintonge, *et al.*, “PHIBSS: Unified Scaling Relations of Gas Depletion Time and Molecular Gas Fractions,” *ApJ* **853**, 179 (2018).
- 11 L. J. Tacconi, R. Genzel, and A. Sternberg, “The Evolution of the Star-Forming Interstellar Medium Across Cosmic Time,” *ARA&A* **58**, 157–203 (2020).
- 12 A. D. Bolatto, M. Wolfire, and A. K. Leroy, “The CO-to-H₂ Conversion Factor,” *ARA&A* **51**, 207–268 (2013).
- 13 E. Peeters, H. W. W. Spoon, and A. G. G. M. Tielens, “Polycyclic Aromatic Hydrocarbons as a Tracer of Star Formation?,” *ApJ* **613**, 986–1003 (2004).
- 14 D. Rigopoulou, H. W. W. Spoon, R. Genzel, *et al.*, “A Large Mid-Infrared Spectroscopic and Near-Infrared Imaging Survey of Ultraluminous Infrared Galaxies: Their Nature and Evolution,” *AJ* **118**, 2625–2645 (1999).
- 15 J. C. Weingartner and B. T. Draine, “Photoelectric Emission from Interstellar Dust: Grain Charging and Gas Heating,” *ApJS* **134**, 263–281 (2001).
- 16 I. García-Bernete, D. Rigopoulou, A. Alonso-Herrero, *et al.*, “A high angular resolution view of the PAH emission in Seyfert galaxies using JWST/MRS data,” *A&A* **666**, L5 (2022).
- 17 I. García-Bernete, D. Rigopoulou, F. R. Donnan, *et al.*, “The Galaxy Activity, Torus, and Outflow Survey (GATOS): V. Unveiling PAH survival and resilience in the circumnuclear regions of AGNs with JWST,” *A&A* **691**, A162 (2024).
- 18 J. J. Jensen, S. F. Hönig, S. Rakshit, *et al.*, “PAH features within few hundred parsecs of active galactic nuclei,” *MNRAS* **470**, 3071–3094 (2017).
- 19 T. S. Y. Lai, L. Armus, M. Bianchin, *et al.*, “GOALS-JWST: Small Neutral Grains and Enhanced 3.3 μm PAH Emission in the Seyfert Galaxy NGC 7469,” *ApJL* **957**, L26 (2023).
- 20 L. Zhang, I. García-Bernete, C. Packham, *et al.*, “Polycyclic Aromatic Hydrocarbon Emission in the Central Regions of Three Seyferts and the Implication for Underlying Feedback Mechanisms,” *ApJL* **975**, L2 (2024).
- 21 J. D. T. Smith, B. T. Draine, D. A. Dale, *et al.*, “The Mid-Infrared Spectrum of Star-forming Galaxies: Global Properties of Polycyclic Aromatic Hydrocarbon Emission,” *ApJ* **656**, 770–791 (2007).
- 22 A. Li, “Spitzer’s perspective of polycyclic aromatic hydrocarbons in galaxies,” *Nature Astronomy* **4**, 339–351 (2020).
- 23 I. Shivaeei and L. A. Boogaard, “The tight correlation between PAH and CO emission from $z \sim 0$ to 4,” *A&A* **691**, L2 (2024).
- 24 Y.-W. Lin, C. K. W. Wu, C.-T. Ling, *et al.*, “Polycyclic aromatic hydrocarbon luminous galaxies in JWST CEERS data,” *MNRAS* **527**, 11882–11892 (2024).
- 25 I. Shivaeei, S. Alberts, M. Florian, *et al.*, “A new census of dust and polycyclic aromatic hydrocarbons at $z = 0.7$ –2 with JWST MIRI,” *A&A* **690**, A89 (2024).
- 26 Y. Gao, Q.-H. Tan, Y. Gao, *et al.*, “The Correlation between WISE 12 μm Emission and Molecular Gas Tracers on Subkiloparsec Scales in Nearby Star-forming Galaxies,” *ApJ* **940**, 133 (2022).
- 27 A. K. Leroy, K. Sandstrom, E. Rosolowsky, *et al.*, “PHANGS-JWST First Results: Mid-infrared Emission Traces Both Gas Column Density and Heating at 100 pc Scales,” *ApJL* **944**, L9 (2023).

- 28 L. Zhang and L. C. Ho, “Estimating Molecular Gas Content in Galaxies from Polycyclic Aromatic Hydrocarbon Emission,” *ApJ* **943**, 1 (2023).
- 29 C. M. Whitcomb, K. Sandstrom, A. Leroy, *et al.*, “Star Formation and Molecular Gas Diagnostics with Mid- and Far-infrared Emission,” *ApJ* **948**, 88 (2023).
- 30 A. Pope, J. Wagg, D. Frayer, *et al.*, “Probing the Interstellar Medium of $z \sim 1$ Ultraluminous Infrared Galaxies through Interferometric Observations of CO and Spitzer Mid-infrared Spectroscopy,” *ApJ* **772**, 92 (2013).
- 31 I. Cortzen, J. Garrett, G. Magdis, *et al.*, “PAHs as tracers of the molecular gas in star-forming galaxies,” *MNRAS* **482**, 1618–1633 (2019).
- 32 A. Kirkpatrick, A. Pope, I. Aretxaga, *et al.*, “Early Science with the Large Millimeter Telescope: Exploring the Effect of AGN Activity on the Relationships between Molecular Gas, Dust, and Star Formation,” *ApJ* **796**, 135 (2014).
- 33 P. F. Goldsmith, “Diffuse Molecular Cloud Densities from UV Measurements of CO Absorption,” *ApJ* **774**, 134 (2013).
- 34 E. da Cunha, B. Groves, F. Walter, *et al.*, “On the Effect of the Cosmic Microwave Background in High-redshift (Sub-)millimeter Observations,” *ApJ* **766**, 13 (2013).
- 35 J. S. Spilker, K. A. Phadke, M. Aravena, *et al.*, “Spatial variations in aromatic hydrocarbon emission in a dust-rich galaxy,” *Nature* **618**, 708–711 (2023).
- 36 A. Moullet, T. Kataria, D. Lis, *et al.*, “PRIMA General Observer Science Book,” *arXiv e-prints*, arXiv:2310.20572 (2023).
- 37 C. M. Bradford, J. Glenn, M. Meixner, *et al.*, “The far-infrared enhanced survey spectrometer (FIRESS) for PRIMA,” in *Space Telescopes and Instrumentation 2024: Optical, Infrared, and Millimeter Wave*, L. E. Coyle, S. Matsuura, and M. D. Perrin, Eds., **13092**, 130920L, International Society for Optics and Photonics, SPIE (2024).
- 38 B. T. Draine, A. Li, B. S. Hensley, *et al.*, “Excitation of Polycyclic Aromatic Hydrocarbon Emission: Dependence on Size Distribution, Ionization, and Starlight Spectrum and Intensity,” *ApJ* **917**, 3 (2021).
- 39 J. S. Mathis, P. G. Mezger, and N. Panagia, “Interstellar radiation field and dust temperatures in the diffuse interstellar medium and in giant molecular clouds,” *A&A* **128**, 212–229 (1983).
- 40 G. B. Rybicki and A. P. Lightman, *Radiative processes in astrophysics* (1979).
- 41 S. Salim and D. Narayanan, “The Dust Attenuation Law in Galaxies,” *ARA&A* **58**, 529–575 (2020).
- 42 B. T. Draine and A. Li, “Infrared Emission from Interstellar Dust. IV. The Silicate-Graphite-PAH Model in the Post-Spitzer Era,” *ApJ* **657**, 810–837 (2007).
- 43 C. Federrath, J. Roman-Duval, R. S. Klessen, *et al.*, “Comparing the statistics of interstellar turbulence in simulations and observations. Solenoidal versus compressive turbulence forcing,” *A&A* **512**, A81 (2010).
- 44 B. Burkhart, M.-Y. Lee, C. E. Murray, *et al.*, “The Lognormal Probability Distribution Function of the Perseus Molecular Cloud: A Comparison of HI and Dust,” *ApJL* **811**, L28 (2015).
- 45 B. Burkhart, D. C. Collins, and A. Lazarian, “Observational Diagnostics of Self-gravitating MHD Turbulence in Giant Molecular Clouds,” *ApJ* **808**, 48 (2015).
- 46 N. Schneider, V. Ossenkopf, T. Csengeri, *et al.*, “Understanding star formation in molecular clouds. I. Effects of line-of-sight contamination on the column density structure,” *A&A* **575**, A79 (2015).

- 47 H. H.-H. Chen, B. Burkhart, A. Goodman, *et al.*, “The Anatomy of the Column Density Probability Distribution Function (N-PDF),” *ApJ* **859**, 162 (2018).
- 48 B. Körtgen, C. Federrath, and R. Banerjee, “The driving of turbulence in simulations of molecular cloud formation and evolution,” *MNRAS* **472**, 2496–2503 (2017).
- 49 E. C. Ostriker, C. F. McKee, and A. K. Leroy, “Regulation of Star Formation Rates in Multi-phase Galactic Disks: A Thermal/Dynamical Equilibrium Model,” *ApJ* **721**, 975–994 (2010).
- 50 S. Bialy, “The Far-UV Interstellar Radiation Field in Galactic Disks: Numerical and Analytic Models,” *ApJ* **903**, 62 (2020).
- 51 A. Rahmati, J. Schaye, A. H. Pawlik, *et al.*, “The impact of local stellar radiation on the H I column density distribution,” *MNRAS* **431**, 2261–2277 (2013).
- 52 P. Padoan, A. Nordlund, and B. J. T. Jones, “The universality of the stellar initial mass function,” *MNRAS* **288**, 145–152 (1997).
- 53 C. Federrath, R. S. Klessen, and W. Schmidt, “The Density Probability Distribution in Compressible Isothermal Turbulence: Solenoidal versus Compressive Forcing,” *ApJ* **688**, L79 (2008).
- 54 N. Murray, E. Quataert, and T. A. Thompson, “On the Maximum Luminosity of Galaxies and Their Central Black Holes: Feedback from Momentum-driven Winds,” *ApJ* **618**, 569–585 (2005).
- 55 T. A. Thompson, E. Quataert, and N. Murray, “Radiation Pressure-supported Starburst Disks and Active Galactic Nucleus Fueling,” *ApJ* **630**, 167–185 (2005).
- 56 C. De Breuck, A. Weiß, M. Béthermin, *et al.*, “A dense, solar metallicity ISM in the $z = 4.2$ dusty star-forming galaxy SPT 0418-47,” *A&A* **631**, A167 (2019).
- 57 C.-W. Tsai, P. R. M. Eisenhardt, J. Wu, *et al.*, “The Most Luminous Galaxies Discovered by WISE,” *ApJ* **805**, 90 (2015).
- 58 K. C. Harrington, R. Fernández Aranda, L. Boogaard, *et al.*, “Hot Diggity Dog: A complete analysis of the extreme molecular gas and dust properties at kpc scales in the hyper-luminous hot, dust-obscured galaxy W2246-0526,” *arXiv e-prints*, arXiv:2504.17639 (2025).
- 59 P. S. Kamieneski, M. S. Yun, K. C. Harrington, *et al.*, “PASSAGES: The Wide-ranging, Extreme Intrinsic Properties of Planck-selected, Lensed Dusty Star-forming Galaxies,” *ApJ* **961**, 2 (2024).
- 60 C. W. Engelbracht, K. D. Gordon, G. H. Rieke, *et al.*, “Metallicity Effects on Mid-Infrared Colors and the $8\ \mu\text{m}$ PAH Emission in Galaxies,” *ApJL* **628**, L29–L32 (2005).
- 61 S. C. Madden, F. Galliano, A. P. Jones, *et al.*, “ISM properties in low-metallicity environments,” *A&A* **446**, 877–896 (2006).
- 62 B. T. Draine, D. A. Dale, G. Bendo, *et al.*, “Dust Masses, PAH Abundances, and Starlight Intensities in the SINGS Galaxy Sample,” *ApJ* **663**, 866–894 (2007).
- 63 J. C. Muñoz-Mateos, A. Gil de Paz, S. Boissier, *et al.*, “Radial Distribution of Stars, Gas, and Dust in Sings Galaxies. II. Derived Dust Properties,” *ApJ* **701**, 1965–1991 (2009).
- 64 K. M. Sandstrom, A. D. Bolatto, C. Bot, *et al.*, “The Spitzer Spectroscopic Survey of the Small Magellanic Cloud ($S^4\text{MC}$): Probing the Physical State of Polycyclic Aromatic Hydrocarbons in a Low-metallicity Environment,” *ApJ* **744**, 20 (2012).
- 65 G. Aniano, B. T. Draine, L. K. Hunt, *et al.*, “Modeling Dust and Starlight in Galaxies Observed by Spitzer and Herschel: The KINGFISH Sample,” *ApJ* **889**, 150 (2020).

- 66 C. M. Whitcomb, J. D. T. Smith, K. Sandstrom, *et al.*, “The Metallicity Dependence of PAH Emission in Galaxies. I. Insights from Deep Radial Spitzer Spectroscopy,” *ApJ* **974**, 20 (2024).
- 67 O. V. Egorov, K. Kreckel, K. M. Sandstrom, *et al.*, “PHANGS-JWST First Results: Destruction of the PAH Molecules in H II Regions Probed by JWST and MUSE,” *ApJL* **944**, L16 (2023).
- 68 R. Maiolino and F. Mannucci, “De re metallica: the cosmic chemical evolution of galaxies,” *A&ARv* **27**, 3 (2019).
- 69 M. Bonato, G. De Zotti, D. Leisawitz, *et al.*, “Origins Space Telescope: Predictions for far-IR spectroscopic surveys,” *PASA* **36**, e017 (2019).
- 70 T. Shibuya, M. Ouchi, and Y. Harikane, “Morphologies of $\sim 190,000$ Galaxies at $z = 0-10$ Revealed with HST Legacy Data. I. Size Evolution,” *ApJS* **219**, 15 (2015).
- 71 T. Morishita, M. Stiavelli, R.-R. Chary, *et al.*, “Enhanced Subkiloparsec-scale Star Formation: Results from a JWST Size Analysis of 341 Galaxies at $5 \leq z \leq 14$,” *ApJ* **963**, 9 (2024).
- 72 T. S. Y. Lai, J. D. T. Smith, E. Peeters, *et al.*, “Spectroscopic Constraints on the Mid-infrared Attenuation Curve. I. Attenuation Model Using Polycyclic Aromatic Hydrocarbon Emission,” *ApJ* **967**, 83 (2024).
- 73 J. S. Mathis, “Interstellar dust and extinction,” *ARA&A* **28**, 37–70 (1990).
- 74 B. T. Draine, *Physics of the Interstellar and Intergalactic Medium* (2011).
- 75 A. Kirkpatrick, A. Pope, A. Sajina, *et al.*, “The Role of Star Formation and an AGN in Dust Heating of $z = 0.3-2.8$ Galaxies. I. Evolution with Redshift and Luminosity,” *ApJ* **814**, 9 (2015).
- 76 S. I. Muldrew, N. A. Hatch, and E. A. Cooke, “What are protoclusters? - Defining high-redshift galaxy clusters and protoclusters,” *MNRAS* **452**, 2528–2539 (2015).
- 77 D. Calzetti, “Star Formation Rate Indicators,” in *Secular Evolution of Galaxies*, J. Falcón-Barroso and J. H. Knapen, Eds., 419, Cambridge University Press (2013).
- 78 S. Liu, X. Z. Zheng, V. Gonzalez, *et al.*, “A first measurement of galaxy merger rate increasing in dynamically colder protoclusters at cosmic noon,” *MNRAS* **536**, 2000–2010 (2025).

Dr. Ilsang Yoon is a scientist at the National Radio Astronomy Observatory. He holds a Ph.D. in Astronomy from the University of Massachusetts Amherst. Dr. Yoon’s research interests include observational study of galaxies and their supermassive black holes in local and distant Universe using primarily radio, millimeter, and far-infrared observing facilities. He has expertise in calibrating radio interferometric data and developing data quality assurance heuristics.